RESEARCH ARTICLE

User Sensing and Localization With Reconfigurable Intelligent Surface for Terahertz Massive MIMO Systems

WEIWEI JIA[1], JIALI CAO [ID][2], (Student Member, IEEE), MEIFENG LI[1], AND ZHIQIANG YU[3]
[1]Xuzhou College of Industrial Technology, Xuzhou 221004, China
[2]State Key Laboratory of Media Convergence and Communication, Communication University of China, Beijing 100024, China
[3]School of Mathematics and Computer Science, Yunnan Minzu University, Kunming 650500, China

Corresponding author: Jiali Cao (cjl_0806@cuc.edu.cn)

ABSTRACT With the evolution of the sixth generation (6G) mobile communication technology, the terahertz (THz) spectrum has attracted much attention in wireless communication applications due to its high bandwidth and low signal transmission delay. However, the introduction of the THz spectrum leads to higher path transmission losses and complex signal attenuation. This makes user sensing and localization in THz massive multiple-input multiple-output (MIMO) systems more challenging. In this paper, we investigate the user sensing and localization problem in THz massive MIMO systems with the assistance of reconfigurable intelligent surfaces (RIS). Firstly, the received signal is modeled as a tensor, and a parallel factor (PARAFAC) method is proposed. The minimum description length (MDL) is then utilized to detect the number of scattering paths in the channel. On this basis, the alternating least squares (ALS) algorithm is employed to estimate the factor matrices, followed by the utilization of a straightforward correlation-based approach to obtain channel parameter information. Finally, the positions of users and scattering points are estimated based on the geometric relationship between channel parameters and location coordinates. The simulation results have verified the effectiveness of the proposed scheme compared to the existing competitive algorithms, and indicate that the proposed scheme exhibits superior parameter estimation performance and can achieve localization accuracy at the decimeter level.

INDEX TERMS Teraherz, massive MIMO, sensing and localization, RIS, tensor.

I. INTRODUCTION

The development of the sixth generation (6G) mobile communication technology has emerged as a focal point in wireless communication technology [1]. Its faster data transmission rate, larger capacity, low communication delay, and support for real-time interaction promote Internet of Things (IoT) connectivity and intelligent applications [2]. The launch of 6G will bring innovations in various application

The associate editor coordinating the review of this manuscript and approving it for publication was Olutayo O. Oyerinde [ID].

scenarios and has enormous potential in the positioning field. Its high-precision positioning capability will drive the development of fields such as smart cities [3], healthcare [4], smart homes [5], and IoT connectivity [6]. For 6G services, the terahertz (THz) spectrum has garnered significant interest owing to its high bandwidth and low signal transmission delay, bringing new possibilities for high-speed data transmission and user perception tracking [7].

However, the emergence of the THz spectrum has also brought a series of new challenges, such as higher path transmission loss, complex signal attenuation, and

difficulties in beamforming [8]. Despite the wide spectrum resources, environmental factors have a significant impact on it, and it is necessary to overcome problems such as signal attenuation. To tackle this concern, reconfigurable intelligent surface (RIS), as a new type of radio spectrum modulation technology, is considered a potential solution to overcome the congestion problem of the THz positioning systems [9]. The RIS adjusts the propagation path and phase of electromagnetic waves by controlling intelligent units on the surface. This method can effectively improve signal quality, reduce transmission losses, and potentially achieve beamforming and interference suppression. Demonstrating the vast potential of creating an intelligent radio environment, the RIS can contribute to the efficient concentration of power at the target receiver by precisely manipulating the phase shift of the reflective elements. Therefore, it is used to enhance the performance of synchronous wireless information and power transmission (SWIPT) systems [10] and multicellular networks [11]. Especially in positioning systems, RIS assistance can improve positioning accuracy [12], [13]. Compared to passive RIS, active RIS has power amplification capability, which can effectively bypass the phenomenon of "dual path loss" and fully tap into the potential of RIS [14]. It should be noted that active RIS is different from traditional relays because it does not require a radio frequency (RF) link.

User sensing and localization play a crucial role in wireless communication. Sensing involves understanding the environment and network conditions of the user equipment (UE), while localization determines the precise location. The main idea of these two is to obtain positional geometric information from channel state information (CSI) measurement, and their accuracy directly influences the performance and service quality of wireless communication systems [15]. Leveraging the sparsity in the angular domain of large-scale multiple-input multiple-output (MIMO) systems, UE localization using the angle of arrival (AOA) has emerged as a focal point of research interest. The work in [16] uses matched filtering and compressed sensing (CS) methods to estimate time of arrival (TOA) and AOA, and utilizes multiple base stations (BS) to perceive the position of the UE. However, this work is not applicable to situations involving a single BS. The authors of [17] give a two-stage algorithm for estimating the CSI. Firstly, the distributed CS synchronous orthogonal matching pursuit (OMP) algorithm is adopted for rough estimation. Then, the expectation maximization algorithm is employed for refinement to perceive the position of indoor terminals. However, the work in [17] requires locating the scatterer to calculate the position of the UE, and is not applicable to the case of a single antenna terminal.

In addition, the utilization of the RIS-assisted UE localization has been widely studied [18], [19], [20], [21], [22]. The work in [18] proposes a near-field target localization algorithm for RIS-assisted positioning systems, which determines the target position by extracting information from RIS-reflected signals. The authors of [19] propose a

superimposed symbol scheme that overlays sensing pilots onto data symbols on the same time-frequency resource. They develop a structure-aware sparse Bayesian learning framework that improves sensing performance and increases spectral efficiency by decoding data symbols as auxiliary information. In [20], the authors introduce an innovative self-sensing RIS architecture, outline the RIS stages, and employ a customized multiple signal classification (MUSIC) algorithm to detect the direction of its nearby target. However, the work in [20] only estimates the angle and cannot obtain the user position. The work in [21] considers the observation degrees of freedom with the assistance of multiple RISs and employs random beamforming and maximum likelihood estimation methods to estimate the angle of departure (AOD) and perceive the UE position. However, this work needs UE to know the location of the RIS, which is difficult to implement in practice. The authors of [22] explores the use of a RIS-assisted millimeter wave (mmWave) MIMO system to estimate the position and rotation angle of a mobile station (MS) in the presence of real scatterers. A two-step localization scheme is proposed that first obtains the channel parameters and then estimates the position-dependent parameters. Simulation results show the superior performance of the proposed localization algorithm.

In wireless communication systems, the CSI obtained through channel estimation is not only the foundation of communication. This information also contains a large amount of sensing information about the transmitter, receiver, and scatterer, such as AOA, AOD, the gain of paths, Doppler frequency shift, displacement, and movement speed. Therefore, a direct connection between communication and sensing can be established naturally. For modern wireless systems functioning at high carrier frequencies such as the mmWave and THz [23], [24], the signal parameter space is essentially multidimensional and may exhibit a multilinear algebraic structure. The tensor dimension can be associated with various signal dimensions, including frequency, time, and space [25], [26]. Tensor decomposition is considered a promising technique for processing large amounts of multidimensional data and has been employed to various communication and sensing systems [27], [28], [29], [30], [31], [32], [33], such as symbol detection, channel estimation, parameter recovery, localization, and mapping. In [29], a third-order parallel factor (PARAFAC) [34] was employed to model the mmWave MIMO orthogonal frequency division multiplexing (OFDM) system. Then two specialized algorithms were developed to estimate the channel with negligible and significant dual broadband effects [35], respectively. The study presented in [30] introduces an optimized nested PARAFAC tensor decomposition method for the simultaneous estimation of sensing parameters and detection of information symbols in time-varying mmWave MIMO systems. This scheme achieves high joint estimation performance without transmitting training sequences, and reduces computational complexity. The work in [31]

describes a tensor decomposition-based approach for time-varying channel estimation in mmWave MIMO-OFDM systems. A fourth-order tensor construction method for low-rank CANDECOMP/PARAFAC (CP) models is proposed and the computational complexity is reduced by optimizing the iteration steps. The study also demonstrates the effectiveness of the proposed method in practical scenarios. The authors of [32] give a joint AOA and flight time estimation scheme for WIFI systems using tensor modeling, and simulation results showed its superiority compared to the existing algorithms. In [33], a tensor-based sensing parameters estimation method is first proposed. These parameters are then utilized to design a search-free localization and mapping method. However, the technique described in [33] is tailored for mmWave systems employing a fully digital beamforming architecture, resulting in an unavoidable increase in power consumption. In addition, the above methods did not consider RIS-assisted scenarios, which enhances communication and sensing performance.

In this paper, we present a user sensing and localization scheme for RIS-assisted THz massive MIMO systems. This scheme is based on the sparsity of THz channels and designs a PARAFAC tensor model for the RIS-assisted THz massive MIMO channel. Subsequently, we utilize minimum description length (MDL) to detect the number of scattering paths in the channel and introduce an alternating least squares (ALS) algorithm for CSI estimation. Specifically, by employing the low-rank property of the received signal tensor and the uniqueness of parallel factorization, the received signal tensor is first decomposed into three factor matrices. Subsequently, a straightforward correlation-based scheme is employed to estimate the channel parameters from the factor matrices. Theoretical research and analysis have been conducted on the uniqueness problem of the constructed tensor model. The proposed algorithm can uniquely estimate channel parameters under more relaxed conditions. Ultimately, leveraging the geometric relationship between the estimated channel parameters and the coordinates of the UE position, the positions of both the UE and scattering points (SP) are determined. The effectiveness of the proposed user sensing and localization scheme is substantiated through simulation results. In comparison to the existing competitive algorithms, the proposed algorithm attains superior channel estimation accuracy with lower complexity.

The subsequent sections of the paper are organized as follows: In Section II, the derivation of the channel model under the RIS-assisted THz massive MIMO system is outlined, representing the received signal as a tensor. Section III proposes a CP decomposition algorithm for the tensor and employs a correlation-based scheme to estimate the channel parameters. The sensing and estimation of the UE and SPs position are realized. Simulation results in Section IV show the effect of system parameters and signal-to-noise ratio (SNR). Section V summarizes the concluding remarks.

Notation: Italic lowercase letters e.g., *b* and boldface lowercase letters e.g., **b** represent scalars and vectors,
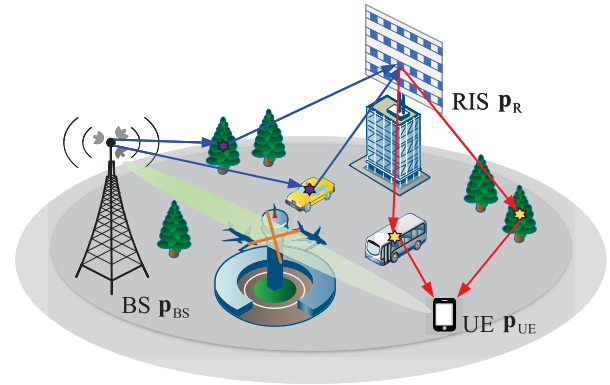

FIGURE 1. Illustration of the considered system model, where the direct channel between the BS and the UE is blocked and communication is carried out through the RIS reflection signals.

respectively. Boldface uppercase letters e.g., $\mathbf{B}$ indicate matrices, while boldface Euler script letters e.g., $\mathcal{B}$ denote tensors. Commonly $\mathcal{B} \in \mathbb{R}^{D_1 \times \cdots \times D_N}$ denotes a N-order tensor. The transpose, Hermitian (conjugate transpose), inverse, pseudo-inverse, and Frobenius norm of a matrix $\mathbf{B}$ are represented as $\mathbf{B}^T$, $\mathbf{B}^H$, $\mathbf{B}^{-1}$, $\mathbf{B}^\dagger$ and $\|\mathbf{B}\|_F$, respectively. The Kronecker product, denoted by $\otimes$, and the Khatri-Rao product (column-wise Kronecker product), represented by $\odot$, are two distinct mathematical operations. The identity matrix of size N and a column vector with all zeros can be denoted by $\mathbf{I}_N$ and $\mathbf{0}_N$, respectively. The notation *diag* ($\mathbf{b}$) is a diagonal matrix, where the main diagonal consists of the entries of $\mathbf{b}$.

II. SYSTEM MODEL

Fig. 1 shows the considered THz massive MIMO-OFDM system, which utilizes RIS to assist communication and sensing between the BS and UE. Since the independence of signals between multiple users in downlink communication, sensing and localization issues in single user scenarios are considered to simplify system design and optimization. The positions of the BS and RIS, denoted as $\mathbf{p}_{BS}$ and $\mathbf{p}_R$ respectively, are predetermined, whereas the position of the UE, represented as $\mathbf{p}_{UE}$, remains uncertain. To facilitate hardware implementation, an analog-digital hybrid beamforming approach is utilized at both the BS and the UE. Both the transmitter and the receiver adopt a Uniform Linear Array (ULA) configuration. The BS utilizes N_B antennas, while the UE is equipped with N_U antennas. The RF links at the BS and UE are M_{BS} and $M_{UE} = 1$, respectively, satisfying $M_{BS} < N_B$ and $M_{UE} < N_U$. RIS consists of N_R units of the same small size, each made of metamaterials that can adjust its reflection coefficient. Assuming the total number of OFDM carriers is $\underline{K}$, for simplification, we select K subcarriers for training.

For the downlink channel, we have considered a single UE. Each subcarrier witnesses the BS employing T distinct beamforming vectors over T consecutive time frames. Within each time frame, the UE utilizes M consecutive RF combination vectors $\mathbf{c}_m$ to detect the transmitted signal, and these vectors are uniform across all subcarriers. Initially,

the received signal is combined within each subframe in the RF domain. Subsequently, after applying the Discrete Fourier Transform (DFT), the cyclic prefix is eliminated, and the symbols undergo conversion back into the frequency domain. The processed received signal associated with the k-th subcarrier ($k = 1, \cdots K$) in the m-th subframe ($m = 1, \cdots M$) can be represented as

$$y_m^k(t) = \mathbf{c}_m^T \mathbf{H}^k \mathbf{q}^k(t) + n_m^k(t), \qquad (1)$$

where $\mathbf{c}_m \in \mathbb{C}^{N_U}$ is the binding vector at the m-th subframe, $\mathbf{H}^k \in \mathbb{C}^{N_U \times N_B}$ is the cascaded channel matrix of the k-th subcarrier, $n_m^k(t)$ is additive Gaussian noise. At the t-th time frame ($t = 1, \cdots T$), $\mathbf{q}^k(t) \in \mathbb{C}^{N_B}$ represents the beamforming vector of the k-th subcarrier, satisfying $\mathbf{q}^k(t) = \mathbf{F}_{RF}(t) \mathbf{F}^k(t) \mathbf{s}^k(t)$, where $\mathbf{F}_{RF}(t)$, $\mathbf{F}^k(t)$, and $\mathbf{s}^k(t)$ represent the RF precoding matrix of all carriers, the digital precoding matrix of the k-th subcarrier, and the pilot symbol vector, respectively.

Collecting signals from M subframes, (1) can be re-represented as

$$\mathbf{y}^k(t) = \mathbf{C}^T \mathbf{H}^k \mathbf{q}^k(t) + \mathbf{n}^k(t), \qquad (2)$$

where $\mathbf{y}^k(t) = [y_1^k(t), \ldots, y_M^k(t)]^T$, $\mathbf{n}^k(t) = [n_1^k(t), \ldots, n_M^k(t)]^T$, and $\mathbf{C} \triangleq [\mathbf{c}_1, \ldots, \mathbf{c}_M] \in \mathbb{C}^{N_U \times M}$.

Assuming that for any $k = 1, \cdots K$, there are $\mathbf{F}^k(t) = \mathbf{F}(t)$ and $\mathbf{s}^k(t) = \mathbf{s}(t)$. Let $\mathbf{S} \triangleq [\mathbf{s}(1), \ldots, \mathbf{s}(T)]$, then the signal received by the UE is represented as

$$\mathbf{Y}^k = \mathbf{C}^T \mathbf{H}^k \mathbf{Q} + \mathbf{N}^k, \qquad (3)$$

where $\mathbf{Y}^k = [\mathbf{y}^k(1), \ldots \mathbf{y}^k(T)] \in \mathbb{C}^{M \times T}$, $\mathbf{N}^k = [\mathbf{n}^k(1), \ldots \mathbf{n}^k(T)]$, and $\mathbf{Q} = [\mathbf{q}(1), \ldots \mathbf{q}(T)] \in \mathbb{C}^{N_B \times T}$. In order to focus on studying the impact of RIS on signal propagation and maintain computational efficiency, we choose a two-dimension channel model [36], which can also be extended to three-dimension models. The representation of the cascaded channel matrix for the k-th subcarrier is as follows [37], [38]:

$$\mathbf{H}^k = \mathbf{H}_{RU}^k \mathbf{\Omega} \mathbf{H}_{BR}, \qquad (4)$$

where $\mathbf{\Omega} = \text{diag}\left(e^{j\omega_1}, \cdots, e^{j\omega_{N_R}}\right) \in \mathbb{C}^{N_R \times N_R}$ is the phase control matrix of the RIS, $\omega_i \in [0, 2\pi]$ is the phase shift coefficient associated with the i-th passive reflecting element. The channel from the BS to the RIS satisfies

$$\mathbf{H}_{BR} = \sum_{l_b=1}^{L_b} \xi_{l_b} \mathbf{a}_R(\overline{\varphi}_{l_b}) \mathbf{a}_B^T(\widetilde{\varphi}_{l_b}). \qquad (5)$$

where ξ_{l_b} represents the complex channel gain of the l_b-th path, $\mathbf{a}_R(\overline{\varphi}_{l_b})$ and $\mathbf{a}_B(\widetilde{\varphi}_{l_b})$ are the steering array vectors of RIS and BS, respectively, and L_b represents the total number of paths between the RIS-BS channel.

Since the fixed positions of the BS and RIS, the channel between the BS and RIS will not undergo significant changes over a period of time, so estimating $\mathbf{H}_{BR}$ is only required once within a brief time period. In addition,
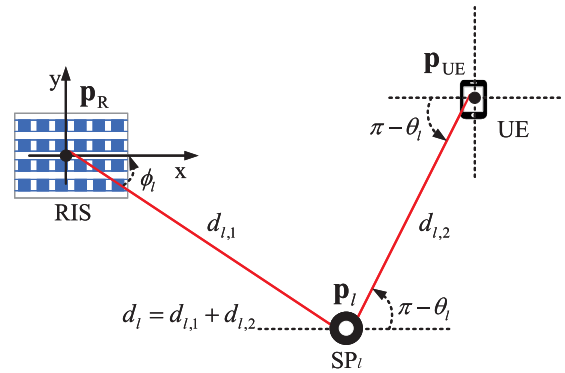

FIGURE 2. Illustration of channel parameters and position coordinates.

based on the assumption of near-static channel and system synchronization, the path delay in (5) can be ignored to simplify the model and focus on the effects of amplitude and phase. Considering the limited scattering of THz waves, the channel $\mathbf{H}_{RU}^k \in \mathbb{C}^{N_U \times N_R}$ between the RIS and UE can be obtained by the superposition of one line-of-sight (LOS) path and $L-1$ non-LoS (NLOS) path [39], as

$$\mathbf{H}_{RU}^k = \sum_{l=1}^{L} \beta_l \exp\left(-j2\pi \tau_l f_s k/\underline{K}\right) \mathbf{a}_M(\theta_l) \mathbf{a}_R^T(\phi_l), \qquad (6)$$

where L represents the number of paths, β_l and τ_l are the complex path gain and time delay of the l-th path ($l = 1, \cdots, L$), f_s is the sampling rate, θ_l and ϕ_l denote the AOA in the UE and the AOD in the RIS on the l-th path, respectively. We calculate the phase shift based on the sampling frequency f_s and normalized frequency k/K to maintain consistency in digital signal processing and simplify model analysis.

1) Path Loss: The path loss in the THz channel consists of molecular absorption loss and diffusion loss [40], i.e. $\beta_l = |\Gamma_l| \left(\frac{c}{4\pi f_c r}\right) e^{-\frac{1}{2}k_{abs}(f_c)r}$. Where c represents the speed of light, r is the LOS path length, f_c denotes the carrier frequency, and $k_{abs}(f_c)$ represents the frequency-dependent absorption coefficient of the medium [41].

Due to its high reflection loss, THz channels have a limited number of NLOS paths and are sparser than mmWave channels. In the THz channel, the gain difference between the LOS path and the NLOS path (averaging over 15 dB [42]) is more prominent than in the mmWave channel. This indicates that THz channels are mainly affected by LOS paths and are more sensitive to obstacles than mmWave channels.

2) Array Response Vector: $\mathbf{a}_M(\theta_l)$ and $\mathbf{a}_B^T(\phi_l)$ respectively represent the antenna array steering vectors for the UE and RIS, both of which satisfy:

$$\mathbf{a}(\psi) = \left[1, e^{-j\frac{d}{\lambda}2\pi \sin(\psi)}, \cdots, e^{-j\frac{d}{\lambda}2\pi(N-1)\sin(\psi)}\right]^T, \qquad (7)$$

where d represents the antenna spacing, λ denotes wavelength, and $\mathbf{a}(\psi) \in \mathbb{C}^{N \times 1}$.

An illustration of the channel parameter concerning the position coordinates is given in Fig. 2, where $d_l = c\tau_l$,

$d_{l,1} = \|\mathbf{p}_l - \mathbf{p}_R\|$ and $d_{l,2} = \|\mathbf{p}_{UE} - \mathbf{p}_l\|$ [43]. The geometric correspondence between channel parameter $\{\tau_l, \theta_l, \phi_l\}$ and position coordinates can be expressed as, with $\mathbf{p}_{UE} = [x_{UE}, y_{UE}]^T$ and $\mathbf{p}_R = [x_R, y_R]^T$

Time delay: $\tau_l = \|\mathbf{p}_l - \mathbf{p}_R\|/c + \|\mathbf{p}_l - \mathbf{p}_{UE}\|/c,$ (8)

AOA: $\theta_l = \pi - \arccos\left((x_{UE} - x_l)/\|\mathbf{p}_{UE} - \mathbf{p}_l\|\right),$ (9)

AOD: $\phi_l = \arccos\left((x_l - x_R)/\|\mathbf{p}_l - \mathbf{p}_R\|\right),$ (10)

where $\mathbf{p}_l = [x_l, y_l]^T$ is the position of the SP associated with the l-th path. Substituting (4) into (3), there are

$$\mathbf{Y}^k = \mathbf{C}^T \mathbf{H}_{RU}^k \mathbf{\Omega} \mathbf{H}_{BR} \mathbf{Q} + \mathbf{N}^k$$
$$= \mathbf{C}^T \mathbf{H}_{RU}^k \mathbf{E} + \mathbf{N}^k, \quad (11)$$

where $\mathbf{E} = \mathbf{\Omega} \mathbf{H}_{BR} \mathbf{Q} \in \mathbb{C}^{N_R \times T}$, $\widetilde{\mathbf{a}}_M(\theta_l) \triangleq \mathbf{C}^T \mathbf{a}_M(\theta_l)$, and $\widetilde{\mathbf{a}}_R(\phi_l) \triangleq \mathbf{E}^T \mathbf{a}_R(\phi_l)$. Combining channels (5) and (6), the received signal $\mathbf{Y}^k$ can be re-represented as:

$$\mathbf{Y}^k = \sum_{l=1}^{L} \beta_l \exp\left(-j2\pi\tau_l f_s k/\underline{K}\right) \mathbf{C}^T \mathbf{a}_M(\theta_l) \mathbf{a}_R^T(\phi_l) \mathbf{E} + \mathbf{N}^k$$
$$= \sum_{l=1}^{L} \beta_l \exp\left(-j2\pi\tau_l f_s k/\underline{K}\right) \widetilde{\mathbf{a}}_M(\theta_l) \widetilde{\mathbf{a}}_R^T(\phi_l) + \mathbf{N}^k. \quad (12)$$

Note that the k-th slice $\mathbf{Y}^k$ of tensor $\mathcal{Y} \in \mathbb{C}^{M \times T \times K}$ is a weighted sum of a common rank-one outer product. Therefore, the tensor $\mathcal{Y}$ facilitates the CP decomposition, which breaks down a tensor into a weighted sum of rank-1 tensors. In other words,

$$\mathcal{Y} = \sum_{l=1}^{L} \widetilde{\mathbf{a}}_M(\theta_l) \circ \widetilde{\mathbf{a}}_R(\phi_l) \circ (\beta_l \mathbf{t}(\tau_l)) + \mathcal{N}, \quad (13)$$

where

$$\mathbf{t}(\tau_l) \triangleq \left[\exp\left(-j2\pi\tau_l f_s \left(1/\underline{K}\right)\right),\right.$$
$$\left.\cdots, \exp\left(-j2\pi\tau_l f_s \left(K/\underline{K}\right)\right)\right]^T. \quad (14)$$

Since the sparse scattering characteristic of the THz channel, the path number L is typically much smaller compared to the tensor dimension. Therefore, the tensor $\mathcal{Y}$ inherently possesses a low-rank structure. This low-rank characteristic guarantees the uniqueness of the CP decomposition of $\mathcal{Y}$ in terms of scaling and arrangement ambiguity. Consequently, through the CP decomposition of the received signal $\mathcal{Y}$, the estimated values of parameters $\{\theta_l, \phi_l, \tau_l, \beta_l\}$ can be obtained. As a result, an estimate of the UE position is acquired. Define

$$\mathbf{U} \triangleq [\widetilde{\mathbf{a}}_M(\theta_1), \cdots, \widetilde{\mathbf{a}}_M(\theta_L)], \quad (15)$$

$$\mathbf{V} \triangleq [\widetilde{\mathbf{a}}_R(\phi_1), \cdots, \widetilde{\mathbf{a}}_R(\phi_L)], \quad (16)$$

$$\mathbf{W} \triangleq [\beta_1 \mathbf{t}(\tau_1), \cdots, \beta_L \mathbf{t}(\tau_L)], \quad (17)$$

where matrices $[\mathbf{U}, \mathbf{V}, \mathbf{W}]$ are factor matrices associated with a noiseless version of $\mathcal{Y}$.

III. THE PROPOSED ALGORITHM

In this section, we derive the PARAFAC decomposition of the tensor form of the received signal. Firstly, we utilize the ALS algorithm to solve the factor matrices of the tensor $\mathcal{Y}$. Then the channel parameter $\{\theta_l, \phi_l, \tau_l, \beta_l\}$ can be estimated through a straightforward correlation-based scheme. And a uniqueness analysis of tensor decomposition is provided. Finally, user sensing and localization are performed based on the estimated parameter information.

A. PARAMETER ESTIMATION

Note that the number of scattering paths L between RIS and UE is typically unknown and requires estimation beforehand. Specifically, the rank of the received signal tensor $\mathcal{Y}$ corresponds to the number of scattering paths L. Therefore, we utilize MDL [44] to detect the rank of tensors. For simplicity, we let $[\mathcal{O}]_j = [\mathcal{Y}]_j^T$ ($j = 1, 2, 3$) represents the transpose of the mode-j unfolding of tensor $\mathcal{Y}$; $I_1 = M$, $I_2 = T$, $I_3 = K$, and $I_T = MTK$. When we perform eigenvalue decomposition on the sample covariance matrix $\frac{I_j}{I_T}[\mathcal{O}]_j[\mathcal{O}]_j^H$, we obtain a set of eigenvalues in descending order $\{\lambda_{1,j}, \cdots, \lambda_{I_j,j}\}$. In the j-th sequential procedure, we utilize the following global eigenvalues for the MDL criterion in detection

$$\lambda_{i,j}^{(G)} = \lambda_{i,1} + \cdots + \lambda_{i,j}, \quad (18)$$

where $i = 1, \cdots, I_j$. Therefore, the estimated value of L is $\widehat{L} = \min\{\widehat{L}_j\}_{j=1}^3$, and we have

$$\widehat{L}_j = \arg\min_{l_j} \text{MDL}\left(l_j\right), \quad (19)$$

$$\text{MDL}\left(l_j\right) = \frac{l_j}{2}\left(2I_j - l_j\right)\log\frac{I_T}{I_j} + p_l\left([\mathcal{O}]_j, \widehat{\rho}_l\right), \quad (20)$$

where $\widehat{\rho}_l$ represents the maximum likelihood estimate of the parameter vector for the l-th model. Additionally, $p_l\left([\mathcal{O}]_j, \widehat{\rho}_l\right)$ denotes the corresponding log-likelihood function, which follows the form [45]

$$p_l\left([\mathcal{O}]_j, \widehat{\rho}_l\right) = \frac{I_T}{I_j}\left(I_j - l_j\right)\log\frac{\frac{1}{I_j - l_j}\sum_{i=l_j+1}^{I_j}\lambda_{i,j}^{(G)}}{\prod_{i=l_j+1}^{I_j}\lambda_{i,j}^{(G)\frac{1}{I_j - l_j}}}. \quad (21)$$

Thus, the CP decomposition of the tensor $\mathcal{Y}$ involves solving the following expression:

$$\min_{\widehat{\mathbf{U}},\widehat{\mathbf{V}},\widehat{\mathbf{W}}} \left\|\mathcal{Y} - \sum_{l=1}^{\widehat{L}}\widehat{\mathbf{u}}_l \circ \widehat{\mathbf{v}}_l \circ \widehat{\mathbf{w}}_l\right\|_F^2. \quad (22)$$

Let $\widehat{\mathbf{U}} = [\widehat{\mathbf{u}}_l, \cdots, \widehat{\mathbf{u}}_{\widehat{L}}]$, $\widehat{\mathbf{V}} = [\widehat{\mathbf{v}}_l, \cdots, \widehat{\mathbf{v}}_{\widehat{L}}]$, and $\widehat{\mathbf{W}} = [\widehat{\mathbf{w}}_l, \cdots, \widehat{\mathbf{w}}_{\widehat{L}}]$. The optimization presented above can be effectively addressed using the ALS algorithm, which can minimize the data fitting error of one factor matrix while

maintaining the other two factor matrices fixed [46].

$$\widehat{\mathbf{U}}^{(t+1)} = \arg\min_{\widehat{\mathbf{U}}} \left\| \mathbf{Y}_{(1)}^T - \left(\widehat{\mathbf{W}}^{(t)} \odot \widehat{\mathbf{V}}^{(t)} \right) \widehat{\mathbf{U}}^T \right\|_F^2, \quad (23)$$

$$\widehat{\mathbf{V}}^{(t+1)} = \arg\min_{\widehat{\mathbf{V}}} \left\| \mathbf{Y}_{(1)}^T - \left(\widehat{\mathbf{W}}^{(t)} \odot \widehat{\mathbf{U}}^{(t+1)} \right) \widehat{\mathbf{V}}^T \right\|_F^2, \quad (24)$$

$$\widehat{\mathbf{W}}^{(t+1)} = \arg\min_{\widehat{\mathbf{W}}} \left\| \mathbf{Y}_{(1)}^T - \left(\widehat{\mathbf{V}}^{(t+1)} \odot \widehat{\mathbf{U}}^{(t+1)} \right) \widehat{\mathbf{W}}^T \right\|_F^2. \quad (25)$$

Note that equations (23) to (25) represent least squares problems, and their solutions can be easily obtained:

$$\widehat{\mathbf{U}}^{(t+1)} = \mathbf{Y}_{(1)} \left[\left(\widehat{\mathbf{W}}^{(t)} \odot \widehat{\mathbf{V}}^{(t)} \right)^T \right]^\dagger, \quad (26)$$

$$\widehat{\mathbf{V}}^{(t+1)} = \mathbf{Y}_{(2)} \left[\left(\widehat{\mathbf{W}}^{(t)} \odot \widehat{\mathbf{U}}^{(t+1)} \right)^T \right]^\dagger, \quad (27)$$

$$\widehat{\mathbf{W}}^{(t+1)} = \mathbf{Y}_{(3)} \left[\left(\widehat{\mathbf{V}}^{(t+1)} \odot \widehat{\mathbf{U}}^{(t+1)} \right)^T \right]^\dagger. \quad (28)$$

Subject to mild conditions, the CP decomposition exhibits uniqueness concerning scaling and arrangement ambiguity. To be more precise, the connection between the estimated factor matrices and the true factor matrices can be expressed as follows:

$$\widehat{\mathbf{U}}^{(\infty)} = \mathbf{U}\boldsymbol{\Lambda}_1\boldsymbol{\Pi} + \mathbf{R}_1, \quad (29)$$

$$\widehat{\mathbf{V}}^{(\infty)} = \mathbf{V}\boldsymbol{\Lambda}_2\boldsymbol{\Pi} + \mathbf{R}_2, \quad (30)$$

$$\widehat{\mathbf{W}}^{(\infty)} = \mathbf{W}\boldsymbol{\Lambda}_3\boldsymbol{\Pi} + \mathbf{R}_3, \quad (31)$$

where $\{\boldsymbol{\Lambda}_1, \boldsymbol{\Lambda}_2, \boldsymbol{\Lambda}_3\}$ is an unknown non-singular diagonal matrix that satisfies $\boldsymbol{\Lambda}_1\boldsymbol{\Lambda}_2\boldsymbol{\Lambda}_3 = \mathbf{I}$; $\boldsymbol{\Pi}$ is an unknown permutation matrix; the estimation errors related to the three estimated factor matrices are represented by $\mathbf{R}_1$, $\mathbf{R}_2$, and $\mathbf{R}_3$, respectively. Ignoring the permutation matrix $\boldsymbol{\Pi}$ is possible since it is consistent across all three factor matrices. Note that each column of $\mathbf{U}$ has a related AOA θ_l. Therefore, an AOA estimation θ_l can be achieved using a straightforward correlation-based approach:

$$\widehat{\theta}_l = \arg\max_{\theta_l} \frac{\left| \widehat{\mathbf{u}}_l^H \widetilde{\mathbf{a}}_{\mathrm{M}}(\theta_l) \right|}{\|\widehat{\mathbf{u}}_l\|_2 \|\widetilde{\mathbf{a}}_{\mathrm{M}}(\theta_l)\|_2}, \quad (32)$$

where $\widehat{\mathbf{u}}_l$ represents the l-th column of $\widehat{\mathbf{U}}$. Given a circularly symmetric Gaussian distribution for the entries in the estimation error matrix $\mathbf{R}_1$, equation (32) serves as a maximum likelihood (ML) estimator. Similarly, the estimated value of the AOD ϕ_l is:

$$\widehat{\phi}_l = \arg\max_{\varphi_l} \frac{\left| \widehat{\mathbf{v}}_l^H \widetilde{\mathbf{a}}_{\mathrm{B}}(\phi_l) \right|}{\|\widehat{\mathbf{v}}_l\|_2 \|\widetilde{\mathbf{a}}_{\mathrm{B}}(\phi_l)\|_2}, \quad (33)$$

where $\widehat{\mathbf{v}}_l$ represents the l-th column of $\widehat{\mathbf{V}}$. When estimating the time delay τ_l from the factor matrix $\widehat{\mathbf{W}}$, it is important to observe that the l-th column of $\mathbf{W}$ is constructed

TABLE 1. The proposed algorithm.

First stage: The Channel Parameters Estimation Algorithm
Input: the received tensor $\boldsymbol{\mathcal{Y}}$, matrices $\mathbf{C}$ and $\mathbf{Q}$, the estimation channel $\widehat{\mathbf{H}}_{\mathrm{BR}}$ between BS and RIS;
1: Obtain eigenvalues by performing eigenvalue decomposition on $\frac{I_j}{I_T}[\mathcal{O}]_j[\mathcal{O}]_j^H$ for all $j = 1, 2, 3$;
2: Compute global eigenvalues by (18);
3: Compute $\widehat{L}_j$ by (19)-(21);
4: Estimation the number of scatter paths L by $\widehat{L} = \min\left\{\widehat{L}_j\right\}_{j=1}^3$;
5: Set $i = 0$ and initialize $\widehat{\mathbf{V}}^{(0)}$ and $\widehat{\mathbf{W}}^{(0)}$ randomly;
6: $t = t + 1$;
7: Compute the least square: $\widehat{\mathbf{U}}^{(t+1)} = \mathbf{Y}_{(1)}\left[\left(\widehat{\mathbf{W}}^{(t)} \odot \widehat{\mathbf{V}}^{(t)}\right)^T\right]^\dagger$;
8: Compute the least square: $\widehat{\mathbf{V}}^{(t+1)} = \mathbf{Y}_{(2)}\left[\left(\widehat{\mathbf{W}}^{(t)} \odot \widehat{\mathbf{U}}^{(t+1)}\right)^T\right]^\dagger$;
9: Compute the least square: $\widehat{\mathbf{W}}^{(t+1)} = \mathbf{Y}_{(3)}\left[\left(\widehat{\mathbf{V}}^{(t+1)} \odot \widehat{\mathbf{U}}^{(t+1)}\right)^T\right]^\dagger$;
10: Repeat steps 6-9 until $\left\|\widehat{\boldsymbol{\mathcal{Y}}}^{(i+1)} - \boldsymbol{\mathcal{Y}}\right\|_F^2 \Big/ \left\|\widehat{\boldsymbol{\mathcal{Y}}}^{(i+1)}\right\|_F^2 \leq \varepsilon$;
11: Estimate the channel parameters $\{\boldsymbol{\beta}, \boldsymbol{\theta}, \boldsymbol{\phi}, \boldsymbol{\tau}\}$ according to (32)-(34);
12: Estimate the channel $\widehat{\mathbf{H}}_{\mathrm{RU}}$ between RIS and UE according to (6);
Output: $\boldsymbol{\beta}, \boldsymbol{\theta}, \boldsymbol{\phi}, \boldsymbol{\tau}, \widehat{\mathbf{H}}_{\mathrm{RU}}$.

using $\beta_l\mathbf{t}(\tau_l)$. Therefore, the expression for estimating the time delay τ_l can be formulated as follows:

$$\widehat{\tau}_l = \arg\max_{\tau_l} \frac{\left| \widehat{\mathbf{w}}_l^H \mathbf{t}(\tau_l) \right|}{\|\widehat{\mathbf{w}}_l\|_2 \|\mathbf{t}(\tau_l)\|_2}, \quad (34)$$

where $\widehat{\mathbf{w}}_l$ represents the l-th column of $\widehat{\mathbf{W}}$. Maximizing problems (32) - (34) involve one-dimensional search, starting with a coarse grid and subsequently refining the search in proximity to potential grid points. Substituting the estimated $\widehat{\theta}_l$ and $\widehat{\phi}_l$ back into (32) and (33) yields the estimated values of the non-singular diagonal matrices $\boldsymbol{\Lambda}_1$ and $\boldsymbol{\Lambda}_2$. Then, the estimated value of $\boldsymbol{\Lambda}_3$ can be obtained through equation $\boldsymbol{\Lambda}_1\boldsymbol{\Lambda}_2\boldsymbol{\Lambda}_3 = \mathbf{I}$. Ultimately, the estimation of the path gain β_l can be achieved using equation (31). Note that the proposed parameter extraction method can also be extended to multi-user three-dimensional scenarios.

The flow of the proposed tensor decomposition and channel parameter estimation algorithm is summarized in **Table 1**, where $\widehat{\boldsymbol{\mathcal{Y}}}^{(i+1)}$ represents the corresponding expansion pattern formed by the estimated three factor matrices $\left\{\widehat{\mathbf{U}}^{(i+1)}, \widehat{\mathbf{V}}^{(i+1)}, \widehat{\mathbf{W}}^{(i+1)}\right\}$ in the $i + 1$-th iteration. ε is the lower limit of error, usually taken as $\varepsilon = 10^{-5}$. Note that the channel between the BS and RIS does not undergo significant changes over a period of time, so we assume that the channel estimated in a short period of time is represented as $\widehat{\mathbf{H}}_{\mathrm{BR}}$.

B. UNIQUENESS ANALYSIS

Within this subsection, the discussion centers around the uniqueness of the CP decomposition. The Kruskal condition [47] ensures the fundamental uniqueness of the CP

TABLE 2. The proposed algorithm.

Second stage: UE Sensing and Localization Algorithm
Input: the position of the RIS $\mathbf{p}_R$, the estimated parameters $\{\boldsymbol{\theta}, \boldsymbol{\phi}, \boldsymbol{\tau}\}$ in **Table 1**.
1: Compute the transmit direction vector $\mathbf{r}_{R,l} = \left[\cos\left(\widehat{\phi}_l\right), \sin\left(\widehat{\phi}_l\right)\right]^T$ and receive direction vector $\mathbf{r}_{UE,l} = \left[\cos\left(\widehat{\theta}_l\right), \sin\left(\widehat{\theta}_l\right)\right]^T$ for the l-th path;
2: Compute the parameters: $\boldsymbol{\delta}_l = \mathbf{p}_R - c\widehat{\tau}_l\mathbf{r}_{UE,l}$;
3: Compute the parameters: $\boldsymbol{\upsilon}_l = c\widehat{\tau}_l\left(\mathbf{r}_{R,l} + \mathbf{r}_{UE,l}\right)$;
4: Estimate the position of the UE $\widehat{\mathbf{p}}_{UE}$ according to (50);
5: Estimate the position of the SP $\widehat{\mathbf{p}}_l$ for path l ($l = 1, \cdots, L$) according to (51);
Output: $\widehat{\mathbf{p}}_{UE}$, $\widehat{\mathbf{p}}_l$ ($l = 1, \cdots, L$).

decomposition. The matrix $\mathbf{O}$ possesses a k-rank, denoted as $k_\mathbf{O}$, defined as the maximum value ensuring the linear independence of each subset with $k_\mathbf{O}$ columns of matrix $\mathbf{O}$. There are the following theorems:

Theorem 1: Let $\{\mathbf{O}, \mathbf{P}, \mathbf{T}\}$ be a CP solution, which decomposes a third-order tensor $\boldsymbol{\mathcal{Z}} \in \mathbb{C}^{S \times G \times J}$ into R rank-1 arrays, where $\mathbf{O} \in \mathbb{C}^{S \times R}$, $\mathbf{P} \in \mathbb{C}^{G \times R}$, and $\mathbf{T} \in \mathbb{C}^{J \times R}$. Assuming the following Kruskal condition hold:

$$k_\mathbf{O} + k_\mathbf{P} + k_\mathbf{T} \geq 2R + 2. \quad (35)$$

Additionally, an alternative CP solution denoted as $\left\{\overline{\mathbf{O}}, \overline{\mathbf{P}}, \overline{\mathbf{T}}\right\}$ exists, which also decomposes the tensor $\boldsymbol{\mathcal{Z}}$ into R rank-1 arrays. Then we have:

$$\overline{\mathbf{O}} = \mathbf{O}\boldsymbol{\Pi}\Lambda_a, \quad (36)$$

$$\overline{\mathbf{P}} = \mathbf{P}\boldsymbol{\Pi}\Lambda_b, \quad (37)$$

$$\overline{\mathbf{T}} = \mathbf{T}\boldsymbol{\Pi}\Lambda_c, \quad (38)$$

where $\boldsymbol{\Pi}$ denotes a transformation matrix, diagonal matrices Λ_a, Λ_b, and Λ_c satisfy $\Lambda_a\Lambda_b\Lambda_c = \mathbf{I}$.

Proof: A strict proof of this can be obtained in [48].

It is crucial to note that the Kruskal condition cannot be realized when $R = 1$. Nevertheless, uniqueness in this scenario has been established by Harshman [49]. For $R = 2$ and $R = 3$, the Kruskal sufficient condition is both necessary and sufficient, but for $R > 3$, it is only sufficient, as indicated by [48].

According to this, we can see that if:

$$k_\mathbf{U} + k_\mathbf{V} + k_\mathbf{W} \geq 2L + 2, \quad (39)$$

then the CP decomposition of the tensor $\boldsymbol{\mathcal{Y}}$ is fundamentally unique. The initial step involves examining the k-rank of $\mathbf{U}$, taking note that:

$$\mathbf{U} = \mathbf{C}^T \left[\mathbf{a}_M\left(\theta_1\right), \cdots, \mathbf{a}_M\left(\theta_L\right)\right] \triangleq \mathbf{C}^T\mathbf{U}_M, \quad (40)$$

where $\mathbf{U}_M \in \mathbb{C}^{N_M \times L}$ a Vandermonde matrix when using a ULA. By generating $\mathbf{C}$ randomly, with its elements uniformly

selected from the unit circle, we can determine the k-rank of $\mathbf{U}$:

$$k_\mathbf{U} = \min\left(N_M, L\right). \quad (41)$$

For the k-rank of $\mathbf{V}$, we have:

$$\mathbf{V} = \mathbf{E}^T\left[\mathbf{a}_R\left(\varphi_1\right), \cdots, \mathbf{a}_R\left(\varphi_L\right)\right] \triangleq \mathbf{E}^T\mathbf{U}_R, \quad (42)$$

where the value of matrix $\mathbf{E}$ immediately falls within the identity circle. The k-rank of $\mathbf{V}$ can be derived:

$$k_\mathbf{V} = \min\left(N_R, L\right). \quad (43)$$

Since the matrix $\mathbf{W}$ satisfies

$$\mathbf{W} = \left[\mathbf{t}\left(\tau_1\right), \cdots, \mathbf{t}\left(\tau_L\right)\right]\mathbf{D}_\beta, \quad (44)$$

where $\mathbf{D}_\beta \triangleq diag\left(\beta_1, \cdots, \beta_L\right)$, it can be shown that the matrix $\mathbf{W}$ is a Vandermonde matrix with cylindrical proportions. Thus, we can obtain the k-rank of $\mathbf{W}$ as follows:

$$k_\mathbf{W} = \min\left(K, L\right). \quad (45)$$

C. USER SENSING AND LOCALIZATION

Let $\mathbf{r}_{R,l} = \left[\cos\left(\widehat{\phi}_l\right), \sin\left(\widehat{\phi}_l\right)\right]^T$ and $\mathbf{r}_{UE,l} = \left[\cos\left(\widehat{\theta}_l\right), \sin\left(\widehat{\theta}_l\right)\right]^T$, represent the transmission direction vector and reception direction vector of the l-th path, respectively. The problem of localization and mapping can be formulated as a maximum likelihood problem:

$$\left[\widehat{\mathbf{p}}_{UE}, [\widehat{\mathbf{p}}_l]_{l=1}^L\right]$$
$$= \arg\max_{\mathbf{p}_{UE}, [\mathbf{p}_l]_{l=1}^L} p\left(\left[\widehat{\tau}_l, \widehat{\theta}_l, \widehat{\phi}_l\right]_{l=1}^L \bigg| \mathbf{p}_{UE}, [\mathbf{p}_l]_{l=1}^L, \mathbf{p}_R\right). \quad (46)$$

To circumvent challenges associated with high-dimensional optimization and hidden parameter inference, we introduce a non-search method rooted in [50]. This approach eliminates the dependence on prior knowledge of path existence. For each cluster l, there are:

$$\mathbf{p}_{UE} = \mathbf{p}_R + c\widehat{\tau}_l\xi_l\mathbf{r}_{R,l} + c\widehat{\tau}_l\left(1 - \xi_l\right)\left(-\mathbf{r}_{UE,l}\right), \quad (47)$$

where the unknown parameter $\xi_l \in [0, 1]$ represents the proportion of the path delay from RIS to the SP of the l-th path. It is essential to emphasize that the value of ξ_l is arbitrary for the LOS path, if it exists. Rearrange (46) that the line equations for each l are:

$$\mathbf{p}_R = \boldsymbol{\delta}_l + \xi_l\boldsymbol{\upsilon}_l, \quad (48)$$

where $\boldsymbol{\delta}_l$ and $\boldsymbol{\upsilon}_l$ satisfy $\boldsymbol{\delta}_l = \mathbf{p}_R - c\widehat{\tau}_l\mathbf{r}_{UE,l}$ and $\boldsymbol{\upsilon}_l = c\widehat{\tau}_l\left(\mathbf{r}_{R,l} + \mathbf{r}_{UE,l}\right)$, respectively. The intersection points of these line segments determine the estimated value of $\mathbf{p}_{UE}$. Specifically, the cost function is represented as the summation of the distances between $\mathbf{p}_{UE}$ and each path:

$$C\left(\mathbf{p}_{UE}\right) = \sum_{l=1}^L \zeta_l \left\|\mathbf{p}_{UE} - \left(\boldsymbol{\delta}_l + \overline{\boldsymbol{\upsilon}}_l^T\left(\mathbf{p}_{UE} - \boldsymbol{\delta}_l\right)\overline{\boldsymbol{\upsilon}}_l\right)\right\|^2, \quad (49)$$
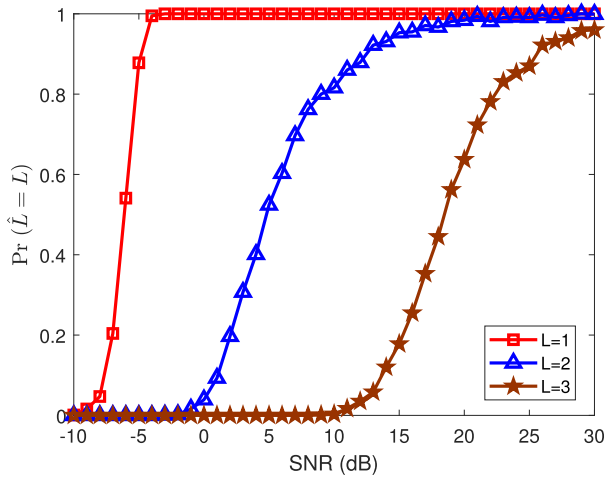
FIGURE 3. PoD versus SNR for different *L*.

where the weight of the *l*-th path $\zeta_l \geq 0$ depends on SNR or path diffusion and $\overline{\boldsymbol{v}}_l = \boldsymbol{v}_l / \|\boldsymbol{v}_l\|$. The least squares solution has become [33]

$$\widehat{\mathbf{p}}_{\text{UE}} = \arg \min_{\mathbf{p}_{\text{UE}}} C \left(\mathbf{p}_{\text{UE}} \right)$$

$$= \left(\sum_{l=1}^{L} \zeta_l \left(\mathbf{I} - \overline{\boldsymbol{v}}_l \overline{\boldsymbol{v}}_l^T \right) \right)^{-1} \sum_{l=1}^{L} \zeta_l \left(\mathbf{I} - \overline{\boldsymbol{v}}_l \overline{\boldsymbol{v}}_l^T \right) \boldsymbol{\delta}_l. \quad (50)$$

Given $\widehat{\mathbf{p}}_{\text{UE}}$, the position $\mathbf{p}_l$ of the SP can be solved as the intersection of the linear equations $\mathbf{p}_R + \rho_R \mathbf{r}_{R,l}$ ($\rho_R \in \mathbb{R}$) and $\mathbf{p}_{\text{UE}} + \rho_{\text{UE}} \mathbf{r}_{\text{UE},l}$ ($\rho_{\text{UE}} \in \mathbb{R}$). The least squares solution is as follows:

$$\widehat{\mathbf{p}}_l = \left(\mathbf{B}_{R,l} + \mathbf{B}_{\text{UE},l} \right)^{-1} \left(\mathbf{B}_{R,l} \mathbf{p}_R + \mathbf{B}_{\text{UE},l} \widehat{\mathbf{p}}_{\text{UE}} \right), \quad (51)$$

where $\mathbf{B}_{R,l} = \mathbf{I} - \mathbf{r}_{R,l} \mathbf{r}_{R,l}^T$ and $\mathbf{B}_{\text{UE},l} = \mathbf{I} - \mathbf{r}_{\text{UE},l} \mathbf{r}_{\text{UE},l}^T$. The flow of the proposed user sensing and localization algorithm is outlined in **Table 2**.

IV. SIMULATION RESULTS

In this section, we evaluate the channel parameter estimation and user sensing performance of the proposed algorithm. The effectiveness of the proposed algorithm is showcased through the results of the Monte Carlo simulation. Define the average probability of detection (PoD) across all Monte Carlo implementations, i.e., $\Pr \left(\widehat{L} = L \right)$, to evaluate the estimation performance of the number of scattering paths *L*. The evaluation of the e1stimation performance of channel parameters, the UE position, and the SPs positions employs the Root Mean Square Error (RMSE), which is defined as:

$$\text{RMSE} (\mathbf{z}) = \sqrt{\frac{1}{N} \left(\sum_{n=1}^{N} \|\widehat{\mathbf{z}}_n - \mathbf{z}_n\|_2^2 \right)}, \quad (52)$$

where $N = 500$ denotes the number of Monte Carlo runs, and *n* signifies the *n*-th independent Monte Carlo run. The

variable $\mathbf{z}$ can refer to the channel parameters $\{\boldsymbol{\beta}, \boldsymbol{\theta}, \boldsymbol{\phi}, \boldsymbol{\tau}\}$, the UE position $\mathbf{p}_{\text{UE}}$, and the SP position $\mathbf{p}_l$ ($l = 1, \cdots, L$). The performance of channel $\mathcal{H}_{\text{RU}} \in {}^{N_U \times N_R \times K}$ estimation is assessed by introducing the Mean Square Error (MSE), which is represented as:

$$\text{MSE} (\mathcal{H}_{\text{RU}}) = \frac{1}{N} \left(\sum_{n=1}^{N} \|\widehat{\mathcal{H}}_{\text{RU},n} - \mathcal{H}_{\text{RU},n}\|_F^2 \right). \quad (53)$$

We define the SNR as [51]:

$$\text{SNR} = 10 \lg \frac{\|\mathcal{Y} - \mathcal{N}\|_F^2}{\|\mathcal{N}\|_F^2}. \quad (54)$$

Taking the following system settings as an example, the channel parameter estimation and user localization performance of the proposed algorithm are demonstrated. In simulation, the communication system should have a carrier frequency of $f_c = 100$GHz, a signal bandwidth of $f_s = 500$MHz, and a total number of carriers of $\underline{K} = 128$. The BS is equipped with 64 antennas, denoted as $N_B = 64$, the UE is equipped with 16 antennas, denoted as $N_U = 16$, and the RIS consists of 32 units, denoted as $N_R = 32$ [52]. Due to the short wavelength of high-frequency signals, such RIS can still effectively adjust the phase of reflected signals, thereby improving signal propagation and enhancing the quality of received signals. It is suitable for specific scenarios such as indoor edge coverage enhancement. There are $L_{\text{BS - RIS}} = 3$ scattering paths between the BS and RIS. The separation between two adjacent antennas is set to half of the signal wavelength.

In the first example, we evaluate the estimation performance of the number *L* of channel scattering paths for different measurements. The relationship between PoDs curves with different reasonable *L* values and SNR is shown in Fig. 3. The remaining system parameters are configured with $M = T = K = 6$. From Fig. 3, it can be seen that PoD increases monotonically with SNR, and for all reasonable numbers of scattering paths *L*, it reaches 1 at sufficiently high SNR.

In the second example, the assessment of the performance of the proposed algorithm in channel parameter estimation and user localization is conducted by varying the number of scattering paths *L* between the RIS and UE. The remaining system parameters are configured with $M = T = K = 6$. Fig. 4 reveals the RMSE curves of the proposed algorithm for estimating channel parameters, the UE position, and the SPs positions at $L = 2$ and $L = 3$. As illustrated in Fig. 4, the RMSE curve exhibits a decreasing trend with the rise in SNR. By decreasing the number of paths *L* between the RIS and UE, there is an enhancement in the estimation performance of the proposed algorithm. The reason is that when the number of paths is small, the multipath effect weakens and the signal becomes more concentrated, thereby reducing the complexity and uncertainty of estimation. The low-rank estimation performance of the proposed algorithm is superior. However, the proposed algorithm exhibits commendable
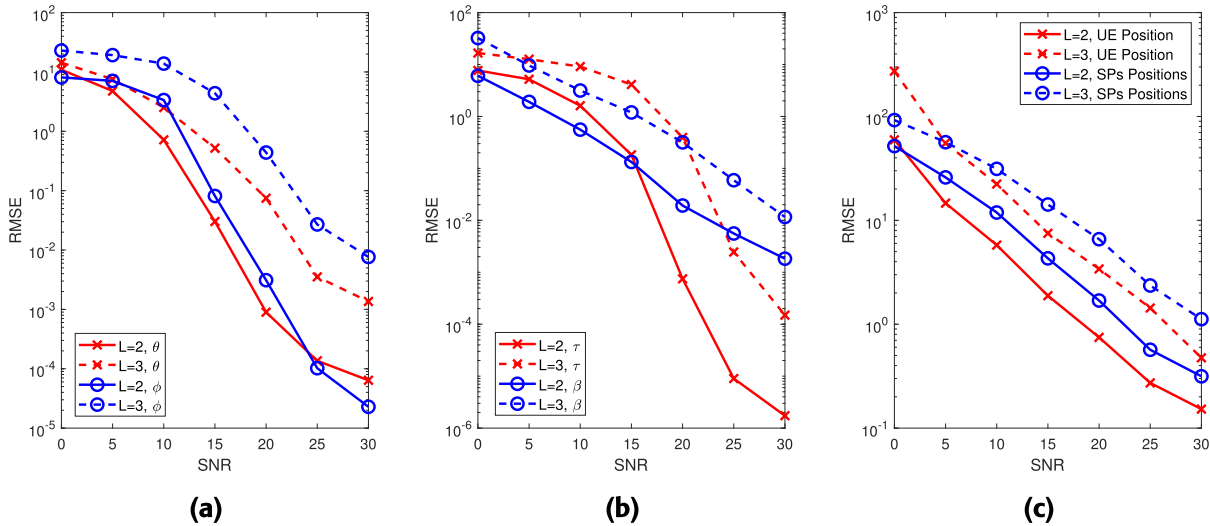
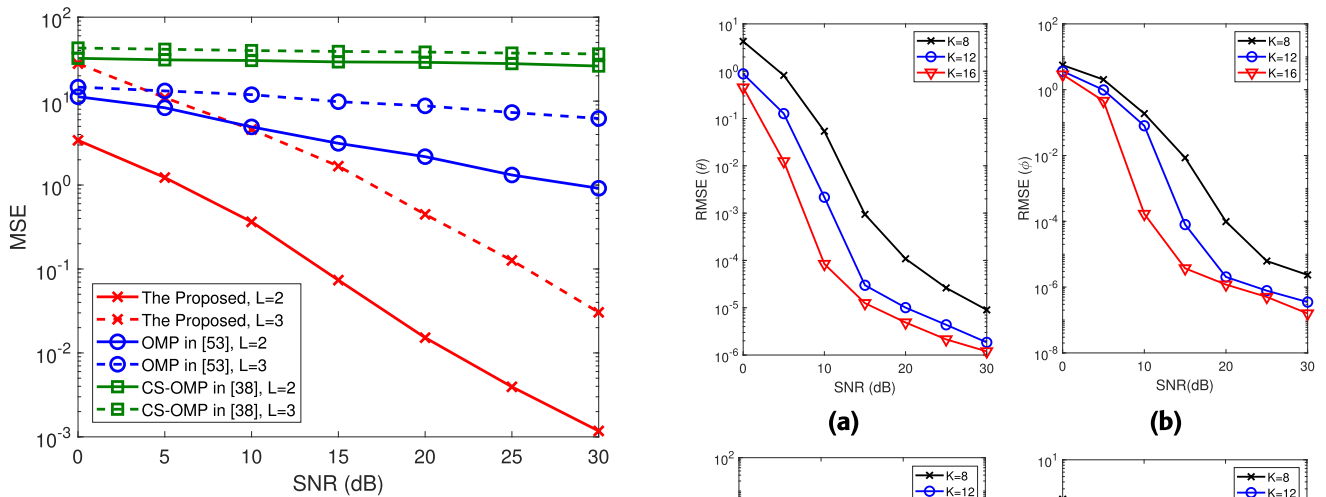**FIGURE 4.** RMSE vs. SNR for the different number of the path.

FIGURE 5. MSE vs. SNR compared with the existing algorithms.

FIGURE 6. RMSE vs. SNR for different K.

channel parameter estimation performance even when $L = 3$. Additionally, the proposed algorithm can implement decimeter-level positioning accuracy. Fig. 5 displays the MSE curves of the estimated channel $\widehat{\mathbf{H}}_{RU}$ for different number of paths and compares them using the OMP algorithm in [53] and the CS-based OMP (CS-OMP) algorithm in [38]. From Fig. 5, it can be seen that when $L = 3$ and SNR $\in [0, 5]$ dB, the estimation performance of the proposed algorithm is inferior to that of OMP. This is because the increase in the number of paths affects the uniqueness of tensor low-rank decomposition, and achieving low convergence accuracy at low SNR. However, even in the presence of multiple paths, the proposed algorithm still has channel estimation performance advantages at medium to high SNR, and exhibits higher accuracy in channel estimation. The above results confirm the effectiveness of the tensor based scheme proposed, as well as the advantages of user localization
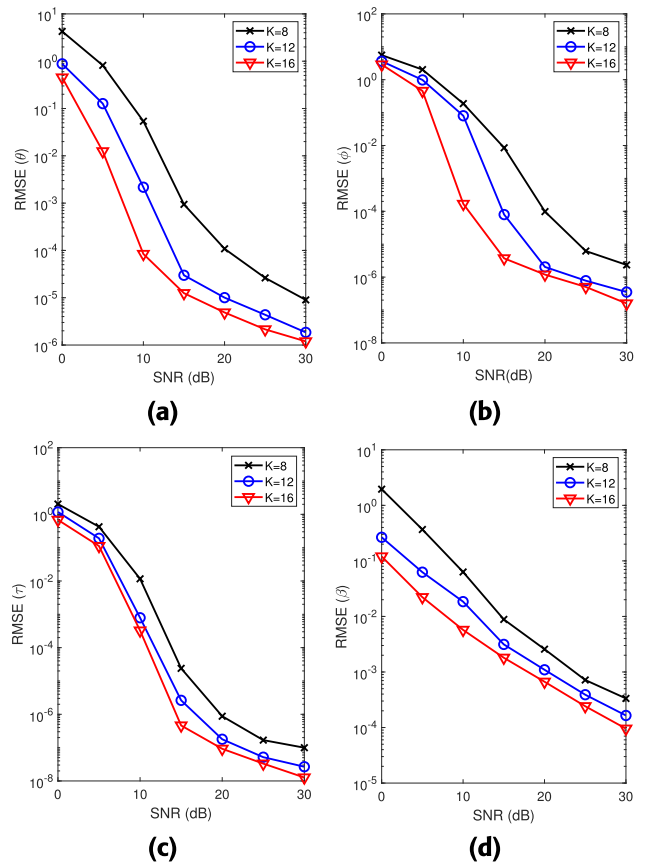
and channel estimation in RIS-assisted THz massive MIMO systems.

In the third example, the evaluation of the performance of the proposed algorithm in implementation parameter estimation and user localization is conducted by varying
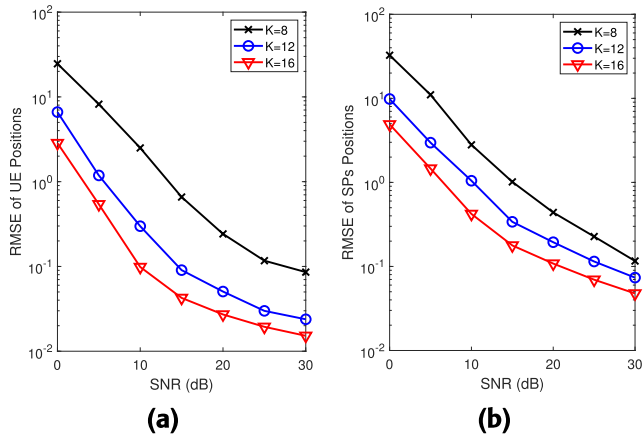
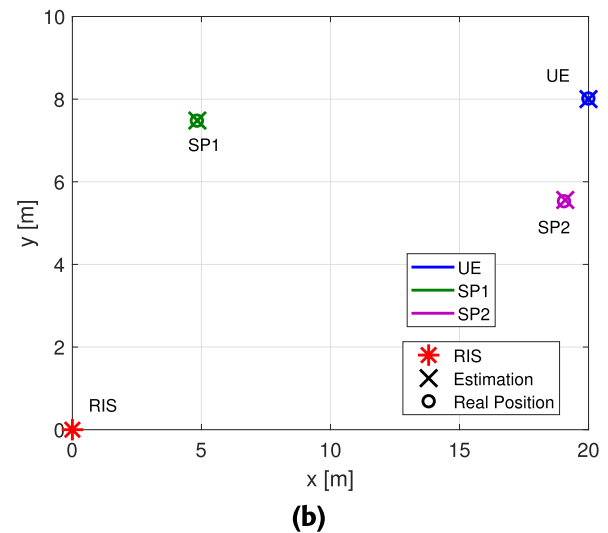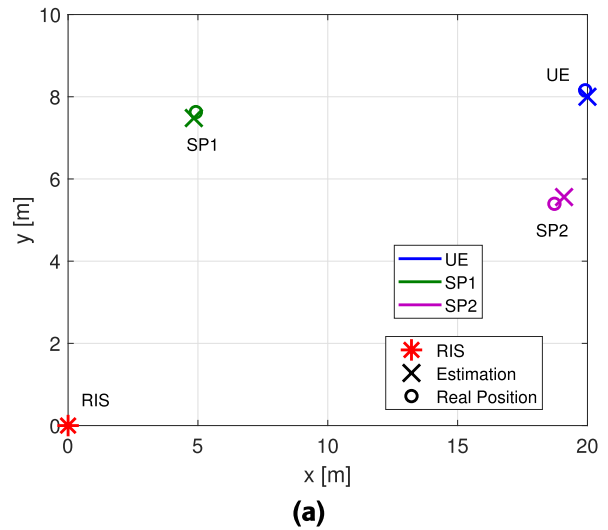**FIGURE 7.** RMSE of the UE and SPs positions vs. SNR for different K.

FIGURE 8. MSE of channel estimation vs. SNR under different number of subcarriers.

FIGURE 9. Two-dimensional mapping diagrams for user sensing and localization of the proposed algorithm. (a) SNR = 10dB; (b) SNR = 25dB.

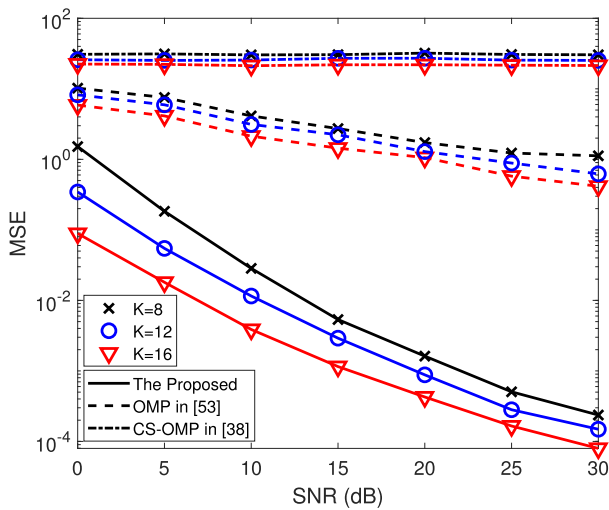the number of subcarriers. We consider the number of subcarriers in three cases: $K = 8$, $K = 12$, and $K = 16$. The remaining system parameters are configured as follows: $M = T = 6$ and $L = 2$. Fig. 6 and Fig. 7 show the RMSE of the proposed algorithm for estimating channel parameter $\{\beta, \theta, \phi, \tau\}$, the UE position, and the SPs positions under different number of subcarriers, respectively. Fig. 8 illustrates the MSE of channel estimation for different number of subcarriers. The observation from Fig. 6 to Fig. 8 indicates that an increase in the number of subcarriers used for training leads to an increase in frequency domain resolution, while the total number of carriers remains constant. The proposed algorithm can more accurately estimate channel parameters and the positions of UE and SPs.

In the final example, we plot a binary map of the proposed algorithm for estimating the positions of the UE and SPs under different SNRs. The remaining system parameters are set as follows: $M = T = 8$, $K = 6$, and $L = 2$. Fig. 9 shows

the binary mapping under SNR = 10dB and SNR = 25dB. From Fig. 9, it can be seen that even at low SNR, the proposed algorithm maintains a commendable level of accuracy in user sensing and localization.

V. CONCLUSION
In this paper, we have introduced a scheme for user sensing and localization in RIS-assisted THz massive MIMO systems. We model the RIS-assisted THz massive MIMO channels as a PARAFAC tensor model. Then the ALS algorithm is utilized for tensor decomposition and estimation of channel parameters. The estimation of channel and user position is finally realized. In comparison to the existing competitive algorithms, the proposed algorithm demonstrates superior accuracy in channel estimation. Moreover, the simulation results illustrate that even with a limited number of subcarriers, the proposed algorithm can still attain localization accuracy at the decimeter level.

REFERENCES

[1] C.-X. Wang, X. You, X. Gao, X. Zhu, Z. Li, C. Zhang, H. Wang, Y. Huang, Y. Chen, H. Haas, J. S. Thompson, E. G. Larsson, M. D. Renzo, W. Tong, P. Zhu, X. Shen, H. V. Poor, and L. Hanzo, "On the road to 6G: Visions, requirements, key technologies and testbeds," *IEEE Commun. Surveys Tuts.*, vol. 25, no. 2, pp. 905–974, 2nd Quart., 2023.

[2] F. Guo, F. R. Yu, H. Zhang, X. Li, H. Ji, and V. C. M. Leung, "Enabling massive IoT toward 6G: A comprehensive survey," *IEEE Internet Things J.*, vol. 8, no. 15, pp. 11891–11915, Aug. 2021.

[3] M. Mohammadi, A. Al-Fuqaha, M. Guizani, and J.-S. Oh, "Semisu-pervised deep reinforcement learning in support of IoT and smart city services," *IEEE Internet Things J.*, vol. 5, no. 2, pp. 624–635, Apr. 2018.

[4] N. B. Gayathri, G. Thumbur, P. R. Kumar, M. Z. U. Rahman, P. V. Reddy, and A. Lay-Ekuakille, "Efficient and secure pairing-free certificateless aggregate signature scheme for healthcare wireless medical sensor networks," *IEEE Internet Things J.*, vol. 6, no. 5, pp. 9064–9075, Oct. 2019.

[5] H. Park, S. Hwang, M. Won, and T. Park, "Activity-aware sensor cycling for human activity monitoring in smart homes," *IEEE Commun. Lett.*, vol. 21, no. 4, pp. 757–760, Apr. 2017.

[6] Y. Zhou, Z. Jin, H. Shi, L. Shi, and N. Lu, "Flying IRS: QoE-driven trajectory optimization and resource allocation based on adaptive deployment for WPCNs in 6G IoT," *IEEE Internet Things J.*, vol. 11, no. 5, pp. 9031–9046, Mar. 2024.

[7] Y. Pan, C. Pan, S. Jin, and J. Wang, "RIS-aided near-field localization and channel estimation for the terahertz system," *IEEE J. Sel. Topics Signal Process.*, vol. 17, no. 4, pp. 878–892, Jul. 2023.

[8] Z. Li, Z. Gao, and T. Li, "Sensing User's channel and location with terahertz extra-large reconfigurable intelligent surface under hybrid-field beam squint effect," *IEEE J. Sel. Topics Signal Process.*, vol. 17, no. 4, pp. 893–911, Jul. 2023.

[9] Y. Han, S. Jin, C.-K. Wen, and T. Q. S. Quek, "Localization and channel reconstruction for extra large RIS-assisted massive MIMO systems," *IEEE J. Sel. Topics Signal Process.*, vol. 16, no. 5, pp. 1011–1025, Aug. 2022.

[10] Y. Pan, K. Wang, C. Pan, H. Zhu, and J. Wang, "Self-sustainable reconfigurable intelligent surface aided simultaneous terahertz information and power transfer (STIPT)," *IEEE Trans. Wireless Commun.*, vol. 21, no. 7, pp. 5420–5434, Jul. 2022.

[11] C. Pan, H. Ren, K. Wang, W. Xu, M. Elkashlan, A. Nallanathan, and L. Hanzo, "Multicell MIMO communications relying on intelligent reflecting surfaces," *IEEE Trans. Wireless Commun.*, vol. 19, no. 8, pp. 5218–5233, Aug. 2020.

[12] T. Wu, C. Pan, Y. Pan, S. Hong, H. Ren, M. Elkashlan, F. Shu, and J. Wang, "Joint angle estimation error analysis and 3D positioning algorithm design for mmWave positioning system," 2022, *arXiv:2208.07602*.

[13] C. Pan, G. Zhou, K. Zhi, S. Hong, T. Wu, Y. Pan, H. Ren, M. D. Renzo, A. L. Swindlehurst, R. Zhang, and A. Y. Zhang, "An overview of signal processing techniques for RIS/IRS-aided wireless systems," *IEEE J. Sel. Topics Signal Process.*, vol. 16, no. 5, pp. 883–917, Aug. 2022.

[14] K. Zhi, C. Pan, H. Ren, K. K. Chai, and M. Elkashlan, "Active RIS versus passive RIS: Which is superior with the same power budget?" *IEEE Commun. Lett.*, vol. 26, no. 5, pp. 1150–1154, May 2022.

[15] F. Liu, Y. Cui, C. Masouros, J. Xu, T. X. Han, Y. C. Eldar, and S. Buzzi, "Integrated sensing and communications: Toward dual-functional wireless networks for 6G and beyond," *IEEE J. Sel. Areas Commun.*, vol. 40, no. 6, pp. 1728–1767, Jun. 2022.

[16] N. Garcia, H. Wymeersch, E. G. Larsson, A. M. Haimovich, and M. Coulon, "Direct localization for massive MIMO," *IEEE Trans. Signal Process.*, vol. 65, no. 10, pp. 2475–2487, May 2017.

[17] A. Shahmansoori, G. E. Garcia, G. Destino, G. Seco-Granados, and H. Wymeersch, "Position and orientation estimation through millimeter-wave MIMO in 5G systems," *IEEE Trans. Wireless Commun.*, vol. 17, no. 3, pp. 1822–1835, Mar. 2018.

[18] M. Luan, B. Wang, Y. Zhao, Z. Feng, and F. Hu, "Phase design and near-field target localization for RIS-assisted regional localization system," *IEEE Trans. Veh. Technol.*, vol. 71, no. 2, pp. 1766–1777, Feb. 2022.

[19] X. Gan, C. Huang, Z. Yang, C. Zhong, X. Chen, Z. Zhang, Q. Guo, C. Yuen, and M. Debbah, "Bayesian learning for double-RIS aided ISAC systems with superimposed pilots and data," 2024, *arXiv:2402.10593*.

[20] X. Shao, C. You, W. Ma, X. Chen, and R. Zhang, "Target sensing with intelligent reflecting surface: Architecture and performance," *IEEE J. Sel. Areas Commun.*, vol. 40, no. 7, pp. 2070–2084, Jul. 2022.

[21] W. Wang and W. Zhang, "Joint beam training and positioning for intelligent reflecting surfaces assisted millimeter wave communications," *IEEE Trans. Wireless Commun.*, vol. 20, no. 10, pp. 6282–6297, Oct. 2021.

[22] S. Hong, M. Li, C. Pan, M. Di Renzo, W. Zhang, and L. Hanzo, "RIS-position and orientation estimation in MIMO-OFDM systems with practical scatterers," 2023, *arXiv:2302.04499*.

[23] X. Yang, M. Matthaiou, J. Yang, C.-K. Wen, F. Gao, and S. Jin, "Hardware-constrained millimeter-wave systems for 5G: Challenges, opportunities, and solutions," *IEEE Commun. Mag.*, vol. 57, no. 1, pp. 44–50, Jan. 2019.

[24] W. Saad, M. Bennis, and M. Chen, "A vision of 6G wireless systems: Applications, trends, technologies, and open research problems," *IEEE Netw.*, vol. 34, no. 3, pp. 134–142, May 2020.

[25] H. Chen, F. Ahmad, S. Vorobyov, and F. Porikli, "Tensor decompositions in wireless communications and MIMO radar," *IEEE J. Sel. Topics Signal Process.*, vol. 15, no. 3, pp. 438–453, Apr. 2021.

[26] J. Du, J. Dong, and F. Gao, "Simultaneous channel estimation and localization of terahertz massive MIMO systems via Bayesian tensor decomposition," *IEEE Commun. Lett.*, vol. 27, no. 2, pp. 541–545, Feb. 2023.

[27] Y. Lin, S. Jin, M. Matthaiou, and X. You, "Conformal IRS-empowered MIMO-OFDM: Channel estimation and environment mapping," *IEEE Trans. Commun.*, vol. 70, no. 7, pp. 4884–4899, Jul. 2022.

[28] X. Yang, W. Liu, and W. Liu, "Tensor canonical correlation analysis networks for multi-view remote sensing scene recognition," *IEEE Trans. Knowl. Data Eng.*, vol. 34, no. 6, pp. 2948–2961, Jun. 2022.

[29] Y. Lin, S. Jin, M. Matthaiou, and X. You, "Tensor-based channel estimation for millimeter wave MIMO-OFDM with dual-wideband effects," *IEEE Trans. Commun.*, vol. 68, no. 7, pp. 4218–4232, Jul. 2020.

[30] J. Du, M. Han, Y. Chen, L. Jin, and F. Gao, "Tensor-based joint channel estimation and symbol detection for time-varying mmWave massive MIMO systems," *IEEE Trans. Signal Process.*, vol. 69, pp. 6251–6266, 2021.

[31] R. Wang, H. Ren, C. Pan, G. Zhou, and J. Wang, "Tensor decomposition-based time varying channel estimation for mmWave MIMO-OFDM systems," 2024, *arXiv:2403.02942*.

[32] B. Zhao, K. Hu, Y. Gong, and Y. Shen, "A tensor-based joint AoA and ToF estimation method for Wi-Fi systems," *IEEE Wireless Commun. Lett.*, vol. 10, no. 11, pp. 2543–2546, Nov. 2021.

[33] F. Wen, J. Kulmer, K. Witrisal, and H. Wymeersch, "5G positioning and mapping with diffuse multipath," *IEEE Trans. Wireless Commun.*, vol. 20, no. 2, pp. 1164–1174, Feb. 2021.

[34] N. D. Sidiropoulos, R. Bro, and G. B. Giannakis, "Parallel factor analysis in sensor array processing," *IEEE Trans. Signal Process.*, vol. 48, no. 8, pp. 2377–2388, Aug. 2000.

[35] B. Wang, F. Gao, S. Jin, H. Lin, G. Y. Li, S. Sun, and T. S. Rappaport, "Spatial-wideband effect in massive MIMO with application in mmWave systems," *IEEE Commun. Mag.*, vol. 56, no. 12, pp. 134–141, Dec. 2018.

[36] L. Wei, C. Huang, G. C. Alexandropoulos, C. Yuen, Z. Zhang, and M. Debbah, "Channel estimation for RIS-empowered multi-user MISO wireless communications," *IEEE Trans. Commun.*, vol. 69, no. 6, pp. 4144–4157, Jun. 2021.

[37] K. Ardah, S. Gherekhloo, A. L. F. de Almeida, and M. Haardt, "TRICE: A channel estimation framework for RIS-aided millimeter-wave MIMO systems," *IEEE Signal Process. Lett.*, vol. 28, pp. 513–517, 2021.

[38] Z. Wan, Z. Gao, F. Gao, M. D. Renzo, and M.-S. Alouini, "Terahertz massive MIMO with holographic reconfigurable intelligent surfaces," *IEEE Trans. Commun.*, vol. 69, no. 7, pp. 4732–4750, Jul. 2021.

[39] K. Dovelos, M. Matthaiou, H. Q. Ngo, and B. Bellalta, "Channel estimation and hybrid combining for wideband terahertz massive MIMO systems," *IEEE J. Sel. Areas Commun.*, vol. 39, no. 6, pp. 1604–1620, Jun. 2021.

[40] W. Yu, Y. Shen, H. He, X. Yu, S. Song, J. Zhang, and K. B. Letaief, "An adaptive and robust deep learning framework for THz ultra-massive MIMO channel estimation," *IEEE J. Sel. Topics Signal Process.*, vol. 17, no. 4, pp. 761–776, Jul. 2023.

[41] H. Yuan, N. Yang, K. Yang, C. Han, and J. An, "Hybrid beamforming for terahertz multi-carrier systems over frequency selective fading," *IEEE Trans. Commun.*, vol. 68, no. 10, pp. 6186–6199, Oct. 2020.

[42] C. Han, J. M. Jornet, and I. Akyildiz, "Ultra-massive MIMO channel modeling for graphene-enabled terahertz-band communications," in *Proc. IEEE 87th Veh. Technol. Conf. (VTC Spring)*, Jun. 2018, pp. 1–5.

[43] J. Du, J. Cao, L. Jin, S. Li, J. Liu, and F. Gao, "Indoor vehicle positioning for MIMO-OFDM WiFi systems via rearranged sparse Bayesian learning," *IEEE Trans. Wireless Commun.*, early access, Dec. 29, 2023, doi: 10.1109/TWC.2023.3345329.

[44] K. Liu, J. P. C. L. da Costa, H. C. So, L. Huang, and J. Ye, "Detection of number of components in CANDECOMP/PARAFAC models via minimum description length," *Digit. Signal Process.*, vol. 51, pp. 110–123, Apr. 2016.

[45] M. Wax and T. Kailath, "Detection of signals by information theoretic criteria," *IEEE Trans. Acoust., Speech, Signal Process.*, vol. ASSP-33, no. 2, pp. 387–392, Apr. 1985.

[46] Z. Zhou, J. Fang, L. Yang, H. Li, Z. Chen, and R. S. Blum, "Low-rank tensor decomposition-aided channel estimation for millimeter wave MIMO-OFDM systems," *IEEE J. Sel. Areas Commun.*, vol. 35, no. 7, pp. 1524–1538, Jul. 2017.

[47] J. B. Kruskal, "Three-way arrays: Rank and uniqueness of trilinear decompositions, with application to arithmetic complexity and statistics," *Linear Algebra Appl.*, vol. 18, no. 2, pp. 95–138, 1977.

[48] A. Stegeman and N. D. Sidiropoulos, "On Kruskal's uniqueness condition for the Candecomp/Parafac decomposition," *Linear Algebra Appl.*, vol. 420, nos. 2–3, pp. 540–552, Jan. 2007.

[49] R. A. Harshman, "Determination and proof of minimum uniqueness conditions for PARAFAC1," *UCLA Working Papers Phonetics*, vol. 22, no. 3, pp. 111–117, 1972.

[50] H. Wymeersch, "A simple method for 5G positioning and synchronization without Line-of-Sight," 2018, *arXiv:1812.05417*.

[51] J. Du, Y. Cheng, L. Jin, and F. Gao, "Time-varying phase noise estimation, channel estimation, and data detection in RIS-assisted MIMO systems via tensor analysis," *IEEE Trans. Signal Process.*, vol. 71, pp. 3426–3441, 2023.

[52] J. Du, Y. Cheng, L. Jin, S. Li, and F. Gao, "Nested tensor-based integrated sensing and communication in RIS-assisted THz MIMO systems," *IEEE Trans. Signal Process.*, vol. 72, pp. 1141–1157, 2024.

[53] P. Wang, J. Fang, H. Duan, and H. Li, "Compressed channel estimation for intelligent reflecting surface-assisted millimeter wave systems," *IEEE Signal Process. Lett.*, vol. 27, pp. 905–909, 2020.

JIALI CAO (Student Member, IEEE) received the B.Sc. degree from the Communication University of China, Beijing, China, in 2022, where she is currently pursuing the M.Sc. degree with the School of Information and Communication Engineering. She has published multiple academic journal articles, including IEEE TRANSACTIONS ON WIRELESS COMMUNICATIONS and IEEE WIRELESS COMMUNICATIONS LETTERS. Her current research interests include sparse Bayesian learning-based techniques, wireless communication, and positioning techniques.

MEIFENG LI received the B.Sc. degree from Xinzhou Teachers University, Xinzhou, China, in 2006, and the M.Sc. degree from Henan Normal University, Xinxiang, China, in 2009. She currently works with the Department of Automotive Engineering, Xuzhou College of Industrial Technology. She has published ten journal articles and conference papers. Her current research interests include wireless communication and wireless sensing technology.

ZHIQIANG YU received the B.S. and M.S. degree in computer science and technology from Yunnan University and the Ph.D. degree in computer science and technology from the Faculty of Information Engineering and Automation, Kunming University of Science and Technology. He is currently working as a Teacher with the School of Mathematics and Computer Science, Yunnan Minzu University. He has led several projects such as the National Natural Science Foundation of China. His research interests include tensor analysis, machine learning and neural network, with emphasis on their application to neural natural language processing, neural machine translation, sensing, and the Internet of Things.

WEIWEI JIA received the B.Sc. degree from Xinzhou Teachers University, Xinzhou, China, in 2006, and the M.Sc. degree from Yunnan University, Kunming, China, in 2009. He currently works with the Department of information engineering, Xuzhou College of Industrial Technology. He has published several journal articles and conference papers. His current research interests include embedded technology and applications, wireless communication, and wireless sensing technology.

• • •